EPJ Photovoltaics

REGULAR ARTICLE

OPEN ACCESS

A study of quenching approaches to optimize ultrasonic spray coated perovskite layers scalable for PV

Joao Silvano[1,2,3,*] (iD), Jacopo Sala[1,2,3], Tamara Merckx[1,3], Yinghuan Kuang[1,3], Pieter Verding[1,2], Jan D'Haen[1,2], Tom Aernouts[1,3], Bart Vermang[1,2,3], and Wim Deferme[1,2]

[1] Imec − Partner in Solliance, Kapeldreef 75, 3000 Leuven, Belgium
[2] Hasselt University, Institute for Materials Research, Wetenschapspark 1, 3590 Diepenbeek, Belgium
[3] EnergyVille, Thor Park 8320, 3600 Genk, Belgium

Abstract. Perovskite materials have gathered increased interest over the last decade. Their rapidly rising efficiency, coupled with the compatibility with solution processing and thin film technology has put perovskite solar cells (PSC) on the spotlight of photovoltaic research. On top of that, band gap tunability via composition changes makes them a perfect candidate for tandem applications, allowing for further harvest of the solar irradiation spectrum and improved power conversion efficiency (PCE). In order to convert all these advantages into large scale production and have increased dissemination in the energy generation market, perovskite fabrication must be adapted and optimized with the use of high throughput, continuous processes, such as ultrasonic spray coating (USSC). In this paper we investigate the ultrasonically spray coated perovskite layers for photovoltaic applications, with particular focus on the quenching-assisted crystallization step. Different quenching techniques are introduced to the process and compared in terms of final layer morphology and cell performance. Finally, gas quenching is used with the large-scale-compatible deposition and allows the production of perovskite solar cells with PCE >15%.

Keywords: Quenching / perovskite / photovoltaic / scalable / spray-coating

1 Introduction

With fast-paced and incremental improvements in efficiency and stability, perovskite solar cells have been consolidated as a critical player in the future of photovoltaic energy generation. Aside for its high performance [1], the band gap tunability granted by the diversity of possible compositions allows the material to be used in alignment with other technologies in multijunction applications. Those can be silicon [2], CIGS [3], and even another type of perovskite [4]. By adding multiple active layers, which can be optimized for absorption of photons of different energy, multijunction devices allow for efficiencies over the Shockley-Queisser limit [5] and perovskite tandem devices are close to reaching the 30% efficiency margin [6]. With the cost of modules dropping, increasing performance (especially efficiency and stability) is the main approach to improve cost-efficiency of photovoltaics applications [7,8].

In the case of dual junction tandems, two cells can be produced independently and mechanically stacked, which is the case of four terminal (4T) devices, or deposited layer by layer monolithically, requiring only two terminals (2T) [9]. While 4T fabrication is less challenging, it also limits the performance due to parasitic absorption and requires transparent electrodes and twice as much external electronics [10]. The set-back of 2T-monolithic devices is the need for a connecting layer for current matching between the cells and to facilitate processing of the second cell, which is done directly on top of the first, on a surface that can be rough, chemical and thermo-sensitive. To overcome these challenges, it is highly beneficial to develop compatible methods, with material deposition by replicable and low-temperature techniques.

The fabrication of a perovskite thin film is most often a two-steps process: the first being the deposition of a precursor solution, where the perovskite components are present as ions in stoichiometric proportions, followed by the crystallization, when the solvent evaporates, and the octahedral crystalline structure is obtained. This step is of crucial relevance to the quality of the formed film. The formation of a crystalline phase initiates when the solution

* e-mail: joao.silvano@uhasselt.be

reaches supersaturation, and hence, is highly dependent on the evaporation rate and choice of solvents [11]. Post processing, such as annealing, is useful to increase grain size. However, the crystallization step does not necessarily require high temperature, owing to the low crystallization activation energy of the material, typically between 50 and $100\,kJ\,mol^{-1}$ [12].

In order to produce a high-quality film, free of pinholes, the crystallization step must be well controlled. Initially, this was done at laboratory scale by solvent quenching, or the anti-solvent technique, which involves the dripping of large amounts of solvents into the precursor solution during spin coating. Problems with replicability, scalability and material waste led to the development of alternative methods, such as vacuum quenching and later, the more industrially viable, gas quenching [13]. Vacuum quenching was demonstrated to produce large area cells with up to 17.86% conversion efficiency [14], while gas quenching is used in a great part of current perovskite fabrication, with a number of devices with PCEs over 20% reported [15]. In the race to commercialization, novel processes, e.g., plasma quenching [16], are associated with high throughput deposition techniques, for instance ultrasonic spray coating and blade coating, to allow a fully roll-to-roll fabrication of perovskite films.

In recent years spray coating, both regular and ultrasonic, has been demonstrated as a suitable deposition method for scalable fabrication of perovskite solar cells [17], with the concept of deposition by spray being employed in some variant methods, such as airbrush [18,19] and sequential spray deposition [20]. In ultrasonic pray coating, the nozzle converts a high frequency electrical signal, fed into electrodes between two piezoelectric transducers, which expand and contract, causing ultrasonic vibrations on the atomizing tip of the nozzle. These vibrations cause the formation of capillary waves on the liquid traveling down the nozzle, and the waves reach a critical amplitude on the atomizing tip, where the liquid is broken into a spray of tiny droplets [21].

In this work we optimize the fabrication of solar cells with a perovskite active layer deposited via quenching-assisted ultrasonic spray coating, with the ultimate goal being the integration of perovskite cells in monolithic tandem devices with copper-indium-selenide/sulfide (CIS) bottom cells. Efficiencies above 14% were achieved with high reproducibility, and champion cell power conversion efficiency (PCE) of 16.88%.

2 Experimental

Initial experiments focused on the optimization of the ultrasonic spray coating parameters. Once full coverage of the substrate was achieved, the deposition of the film was further studied by using it as the active layer of a single junction solar cell.

The optimization of the ultrasonic spray coating of perovskites was conducted by depositing perovskite precursor solutions on plain $1\,in^2$ glass substrates (from Marienfeld Superior). During this step, different solution compositions and ultrasonic spray coating parameters were

tested. The selection of perovskite components was done based on simulations for optimal performance of monolithic 2T devices with CIS (1.0 eV) as bottom cell; as such the perovskite film must have a bandgap between 1.60 and 1.65 eV [22], which is tuned by controling the proportion of iodide (I^-) and bromide (Br^-) in the precursor solution. Moreover, a double-cation composition, with cesium (Cs^+) and formamidinium (FA^+), was selected, avoiding stability issues associated with commonly used methylammonium (MA^+) [23]. The final perovskite composition is $Cs_{0.18}FA_{0.82}Pb(I_{0.94}Br_{0.06})_3$.

2.1 Solution formulation

The precursor solutions were prepared by diluting lead(II) iodide (PbI_2) (from TCI), formamidinium iodide (FAI) (from DYESOL) and cesium bromide (CsBr) (from abcr) in Dimethylformamide (DMF) and N-Methyl-2-Pyrrolidone (NMP) (both from Sigma Aldrich). Concentrations ranged from 1.33 M to 0.25 M, and solvent volumetric proportions from DMF-only (1:0) to 4:1 DMF:NMP. The solution is stirred for a minimum of 24h before use. All handling is conducted in controlled environments (N_2-filled glove box or dry room).

2.2 Device fabrication

The solar cells follow a p-i-n architecture. They were produced ITO coated glass (Colorado Concept) substrates. A nickel oxide (NiOx) hole transport layer of 15 nm is deposited on the substrate by sputtering from a nickel metallic target under O_2 plasma using a Nebula linear sputtering system (from Angstrom Engineering Inc.) and subsequently annealed at $300\,^\circ C$ in air for 20 min. The next step is perovskite deposition. The previously described precursor solution is deposited by ultrasonic spray coating with a rate of 1 mL/min, nozzle power of 3 W. The ultrasonic spray coater (from Sono-Tek) is equipped with an Impact nozzle, in which the ultrasonicated mist is projected to the substrate by an auxiliary N_2 flow (3 psi). During the deposition the substrate is kept on top of a $40\,^\circ C$ hotplate. The nozzle is positioned 10 cm away from the sample and passes through it with a speed of 30 mm/s. These parameters were selected after optimization studies described in the next section and are used for all samples unless stated otherwise. Vacuum quenching was done by transferring the sample with a wet film to an N_2 filled chamber and creating vacuum with a pump, taking around 1 min for it to reach a steady state. Gas quenching was performed by applying a N_2 flow to the wet film at an angle of 90°, the N_2 flow has a maximum pressure of 8 psi and can be controlled with an air gun. After deposition and optional quenching, the perovskite films are annealed at $100\,^\circ C$ for 30 min to completely eliminate solvents.

The electron transport layers (ETL) and metallic electrode are then thermally evaporated (deposition tools from Angstrom Engineering Inc.). The ETL is a triple layer of lithium fluoride (LiF), buckminsterfullerene (C60) (from Nano-C) and bathocuproine (BCP) (from Lumtech). The metallic electrode is a 100 nm layer of copper (Cu)
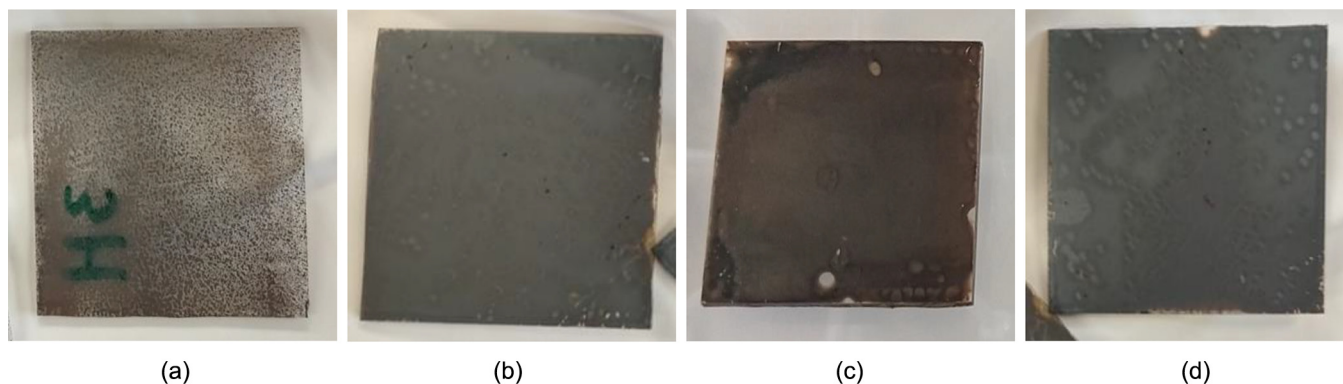
Fig. 1. Ultrasonically spray coated perovskite samples. Heterogeneous coverage as result of high processing temperature and absence of NMP (a). Opaque layers as result of slow solvent evaporation (b,c,d).

deposited after mechanical etching to partially expose the ITO. The copper is deposited with the aid of a 16 rectangles mask, in which 4 of those (deposited over the exposed ITO) function as the bottom contact, while the rest function as top electrodes. The areas where copper overlaps the patterned ITO gives origin to 12 cells of 0.125 cm^2 active area.

Both plain glass and ITO coated glass substrates were cleaned before use in an ultrasonic bath in sequential solutions of soap, water, acetone and isopropyl alcohol (IPA). The substrates are then dried with a N_2 gun and go through a final cleaning step of UV-Ozone treatment for 15 min, which also improves the wettability of the substrates. After cleaning, all processing is conducted inside N_2-filled glove boxes.

2.3 Characterization

Optical and laser imaging was performed with a KEY-ENCE VK-X 250 3D laser scanning confocal microscope. Scanning electron microscopy (SEM) analysis was performed with a FEI Quanta 200 FEG-SEM.

The performance of solar cells is determined by JV measurements using a solar simulator with an Xe arc lamp light source (from Abet technology), under one sun AM 1.5G irradiation, and with a Keithley 2602A source meter. All performance characterization is performed in controlled environments (N_2-filled glove box). A cooling fan is used to maintain the cells at room temperature during measurements. External quantum efficiency (EQE) measurements are performed with a Bentham PVE300 spectral response setup with halogen and Xenon lamps.

3 Results and discussion

3.1 Ultrasonic spray coating of perovskite

The initial experiments with the ultrasonic spray coater focused on obtaining an homogeneous perovskite layer, covering the entire surface of the sample (1 inch^2 glass), and comparing it to spin coated layers. Since the scalable technique has less material waste than spin coating, the

precursor solution concentration was initially reduced from the usual 1.33 M to 0.25 M. The molecular composition $(Cs_{0.18}FA_{0.82}Pb(I_{0.94}Br_{0.06})_3)$ was used to achieve the desired band gap of 1.6 eV. To study the effects of evaporation time, two solvents were employed in varying proportions − Dimethylformamide (DMF) as high volatile solvent, and N-Methyl-2-Pyrrolidone (NMP) as low volatile solvent. Processing temperature was also studied by controlling the hot plate temperature in which the sample was positioned during deposition (from room temperature to 100 °C). Perovskite crystallization occurs after the precursor solution reaches the saturation point. Thus, it is important to have a complete wet film deposited before the solution reaches the saturation point on the surface of the substrate.

Both in cases of high temperatures (higher than 60 °C) and absence of NMP, premature crystallization was detected, meaning that the solution couldn't settle homogeneously on the substrate prior to the crystallization. As such, heterogeneous coverage could be verified (Fig. 1a). In extreme cases the solvent evaporates before reaching the glass, resulting again in heterogeneous coverage and possibly non-crystallized precursor powder being deposited on the sample.

Processing at room temperature and with the addition of low volatile NMP allows for a slower evaporation of the solvent and results in fully covered samples. Still, the resulting film differs significantly from spin-coated ones in both coloration and transparency. The ultrasonically spray coated layer was opaque and grey (Figs. 1b–1d) while spin coated layers are partially reflective and have brown coloration. This could indicate a high roughness and thickness for the USSC perovskite. Optical and laser imaging was used to investigate the layer further and revealed the agglomeration of perovskite material into fiber-like structures (Fig. 2).

The 3D laser scanning confirmed the expected high roughness, with spots of glass left completely uncovered. The stacked fiber-like structures also generate a highly-porous layer instead of the packed grains usually seen in crystalline perovskite for photovoltaic applications. Additionally, by drying slowly at room temperature, the solvent

Fig. 2. Fiber-like structures observed by optical microscopy after the ultrasonic spray coating of perovskite with slow solvent evaporation.

evaporates with different rates in the center and edges of the sample, which can create agglomeration of material in localized spots. The same happens when increasing the temperature of the hot plate after deposition, although the complete drying is faster. In order to avoid the issues related to slow drying, while also allowing the formation of a wet layer on the sample, auxiliary quenching techniques were employed.

Both vacuum and gas quenching after ultrasonic spray coating resulted in faster crystallization, with brown semi-transparent films (Fig. 3) resembling the spin-coated perovskite. The maximum resolution of the VK-X 250 3D laser scanning confocal microscope does not allow for observation of the perovskite grains, being only possible to visualize smaller surface defects or impurities in the quenched films (Fig. 4). Nevertheless, the technique reveals reduced surface roughness and a more compact crystalline film, as well as the absence of elongated fiber-like structures. Further details and comparison between the two techniques are discussed in the next sections.

3.2 Vacuum quenching

Low temperature deposition of a precursor solution of 4:1 DMF:NMP volumetric proportion was used to obtain the wet layer. The hot plate temperature was kept at $40\,°C$ to eliminate variations of room temperature. It was observed that with these conditions the wet layer reaches super-saturation only after a few minutes, enough time to apply the auxiliary quenching technique.

As the first attempted quenching technique, vacuum quenching was responsible for a significant improvement in film quality. The VK-X 250 3D laser scanning showed an average thickness of $609\,nm$ − similar to the desired thickness of spin coated samples − and a roughness lower than $35\,nm$.

With the perovskite deposition on glass reaching the desired morphology, the next step was fabricating single junction cells with the spray coated layer, as indicated in the experimental section. In order to optimize the vacuum
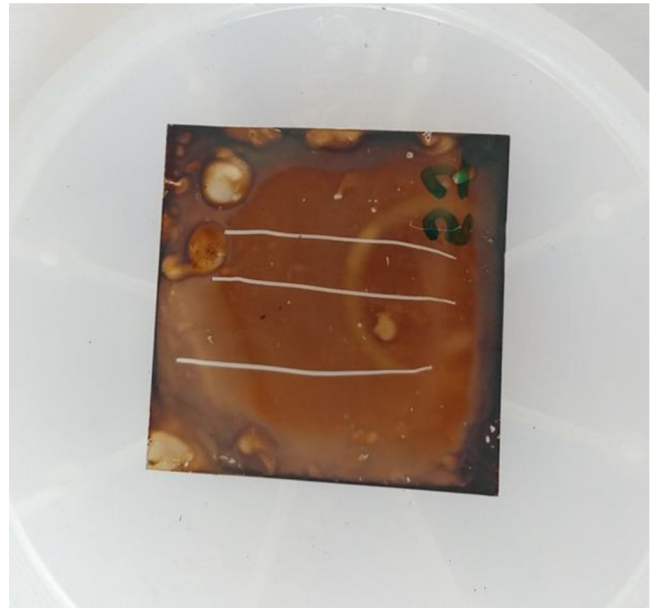

Fig. 3. Ultrasonically spray coated perovskite sample after undergoing vacuum quenching for accelerated crystallization. Stripes were made for the purpose of thickness measurements.
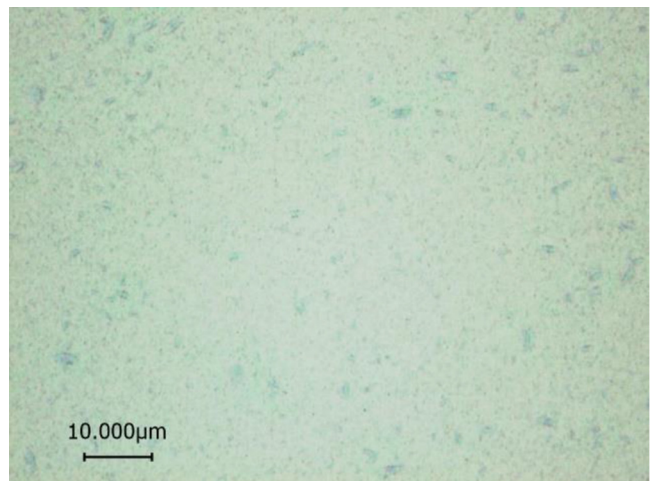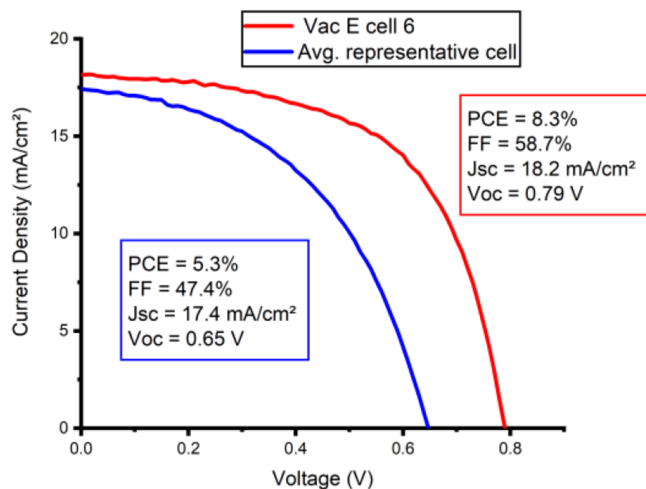

Fig. 4. Ultrasonically spray coated perovskite layer after vacuum quenching and annealing. The perovskite completely covers the glass substrate, being only possible to observe the defects on top of the perovskite surface.

quenching, 10 samples were produced with varied exposure time under vacuum. The first 4 samples (Vac A, B, C and D) presented incomplete quenching, with solvent remaining in the central region of the sample, those were inside the vacuum chamber for 1, 10, 20 and $60\,s$, respectively, after the chamber reached its vacuum steady state. Samples Vac E, F and G were in vacuum for $180\,s$, and samples Vac H, I and J for $120\,s$. All of the 6 last samples were completely quenched, with no excess solvent visible in the substrate, and didn't exhibit significant visual difference among themselves, possibly indicating no addi-

Table 1. Average performance of perovskite solar cells fabricated by USSC and vacuum quenching (with standard deviation).
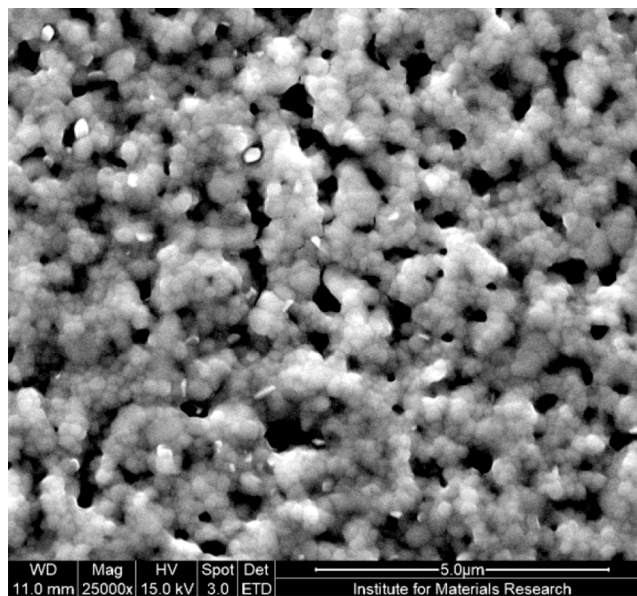
Sample	V_{oc} (mV)	J_{sc} (mA/cm^2)	FF (%)	η (%)
Vac E	675 ± 62	18.3 ± 0.4	48.5 ± 5.2	6.0 ± 1.1
Vac F	558 ± 20	18.1 ± 0.3	47.5 ± 2.7	4.8 ± 0.4
Vac G	584 ± 25	18.2 ± 0.4	44.3 ± 2.8	4.7 ± 0.5
Vac H	651 ± 48	18.4 ± 0.5	46.6 ± 3.3	5.6 ± 0.9
Vac I	628 ± 35	18.1 ± 0.4	45.9 ± 3.8	5.3 ± 0.8
Vac J	605 ± 34	17.8 ± 0.4	49.2 ± 3.9	5.3 ± 0.6

Fig. 5. J–V curves of champion and average-representative cells obtained with vacuum quenching. For the average-representative cell, the one with closest performance to the average values was chosen.

Fig. 6. Perovskite layer morphology after ultrasonic spray coating and vacuum quenching.

tional effect after 2 min of vacuum. The resulting 72 cells (6 samples × 12 cells per sample) had their performance tested by J-V analysis, which allows for the determination of the short-circuit current (J_{sc}), open circuit voltage (V_{oc}), fill factor (FF) and power conversion efficiency (PCE). A summary of the sample results is given in Table 1.

The lack of discernable patterns between cells E–G and H–J agrees with the conclusion that after 2 min the samples were completely quenched. The variation between samples can be attributed to handling of the sample while still having the deposited wet layer. The movement required to transfer the samples from the spray coater hot plate to the vacuum chamber can cause localized flow of the precursor solution and introduce randomness to the process.

The average PCE was 5.30% ($\sigma = 0.87\%$), with top cell performance being: PCE = 8.3%, $V_{oc} = 790$ mV, $J_{sc} = 18.2$ mA/cm^2, FF = 58.7% (sample Vac E, cell 6) (Fig. 5). These results are far from the typical values for spin coated perovskites, possibly due to the long time required in the vacuum system for quenching, which translates into slow crystallization and generates porous films. SEM imaging confirmed this characteristic (Fig. 6). While optimizing the vacuum chamber size and increasing

the pump power could lead to faster solvent elimination, the lack of scalability and issues with reproducibility resulted in the search for another quenching technique.

3.3 Gas quenching

Gas quenching offers high scalability and compatibility with roll-to-roll production, while having lower investment and operational costs if compared with vacuum quenching. Having a N$_2$ line already attached to the USSC setup, it was also possible to perform in situ quenching, without the need to transport the sample.

The fabrication of gas-quenched cells followed the same spray coating parameters utilized before, depositing a layer of precursor solution (solvent mixture of 4:1 DMF:NMP) at 40 °C. The 8 psi N$_2$ pressure used in the gas quenching of spin-coated cells was reduced to 4 psi in order to avoid material loss, since the lack of the spinning motion results on a thicker wet layer after spray coating. In the quenching process the formation of crystals on the sample is easily verified by the color change: from the transparent yellow
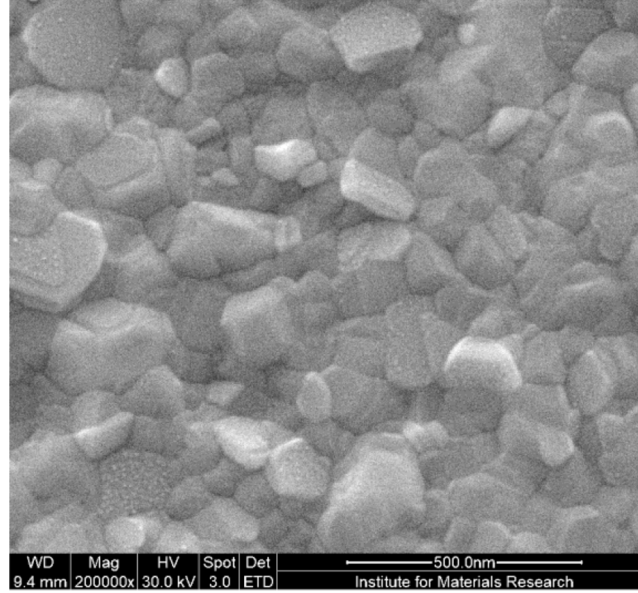
Fig. 7. Perovskite layer morphology after ultrasonic spray coating and gas quenching.

Table 2. Average performance of perovskite solar cells fabricated by USSC, with additional vacuum (control sample) and gas quenching (with standard deviation).

Sample	V_{oc} (mV)	J_{sc} (mA/cm^2)	FF (%)	η (%)
N2 1A	888 ± 25	17.2 ± 0.3	71.1 ± 2.6	10.8 ± 0.7
N2 1B	868 ± 06	15.9 ± 0.6	75.7 ± 1.7	10.5 ± 0.4
N2 1C	863 ± 08	16.4 ± 0.4	74.9 ± 2.5	10.6 ± 0.3
N2 1D	845 ± 13	16.9 ± 0.3	70.2 ± 1.7	10.0 ± 0.4
N2 1E	868 ± 21	17.6 ± 0.7	71.6 ± 1.7	10.9 ± 0.6
N2 1F	854 ± 25	18.0 ± 1.0	68.8 ± 2.5	10.6 ± 1.2
N2 1G	852 ± 17	17.6 ± 0.7	71.9 ± 4.2	10.8 ± 0.4
Vac ctrl	658 ± 44	17.1 ± 0.3	56.4 ± 4.3	6.4 ± 0.9

film to a dark brown reflective thin layer. In spin coated samples, the change starts a few seconds after exposure to the gas flow, and after 10 s no further color change is observed, indicating complete quenching. Due to lower nitrogen pressure, the ultrasonically spray coated samples exhibited longer crystallization periods, taking around 25 s before the entire surface reached a steady color. Nevertheless, the crystallization was faster than with vacuum quenching. SEM imaging shows a compact crystalline layer (Fig. 7) without the presence of the holes seen in vacuum quenched layers.

In the first experiment, 8 samples were produced, for a total of 96 cells. One of the samples was fabricated with vacuum quenching for control over different batches and had results compatible to the previously seen range (Tab. 2). The average PCE for the first N2 quenched cells was 10.61% ($\sigma = 0.66\%$). The top performing cell had a PCE = 13.26%, $V_{oc} = 900\,\mathrm{mV}$, $J_{sc} = 19.7\,\mathrm{mA/cm^2}$, FF = 74.74% (sample N2 1F, cell 12) (Fig. 8). Additionally, external quantum efficiency (EQE) measurements were used to calculate the bandgap of the cell using the inflection point of the EQE
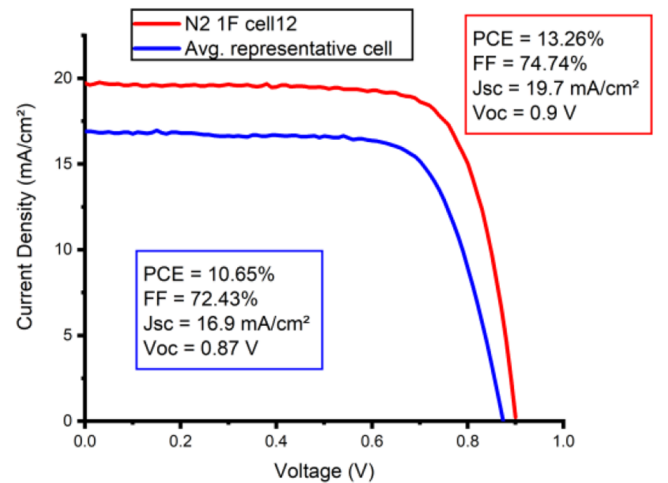

Fig. 8. J–V curve of champion and average-representative cells obtained with low pressure gas quenching. For the average-representative cell, the one with closest performance to the average values was chosen.
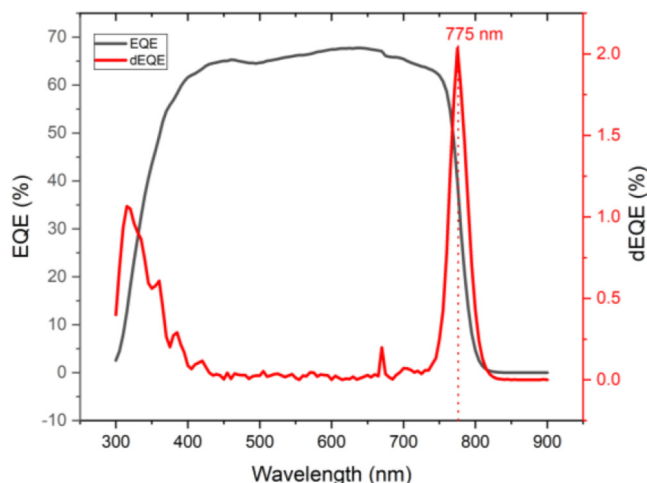
Fig. 9. External quantum efficiency (EQE) measurements and determination of the inflection point.

Table 3. Average performance of perovskite solar cells fabricated by USSC and high pressure gas quenching, with 0.5 M solution (with standard deviation).

Sample	V_{oc} (mV)	J_{sc} (mA/cm^2)	FF (%)	η (%)
N2 2A	953 ± 23	19.4 ± 0.3	71.9 ± 2.2	13.3 ± 0.6
N2 2B	951 ± 25	19.1 ± 0.7	70.7 ± 3.0	12.8 ± 1.2
N2 2C	944 ± 20	19.0 ± 0.5	74.5 ± 2.3	13.4 ± 0.7
N2 2D	948 ± 07	18.4 ± 0.9	75.8 ± 1.7	13.2 ± 0.8
N2 2E	957 ± 08	18.1 ± 0.5	75.74 ± 2.3	13.1 ± 0.7

curve, as described in Krückemeier et al. [24]. As shown in Figure 9, the inflection point occurs at wavelength $(\lambda) = 775$ nm. This value is then used to calculate the bandgap (E_g) following the derivation of Plank's equation: E_g (eV) $= 1240/\lambda = 1.6$ eV. Due to the collection of data for every 5 nm wavelength the error of this method is ± 0.01 eV. Nevertheless, it is possible to verify that the bandgap of the cell is near the desired value of 1.6 eV, ideal for tandem applications with CIS bottom cells.

Aiming to test the higher gas pressure and unlock faster quenching, alternative routes were considered. A solution with 0.5 M concentration (twice as much precursor material) was used to compensate the material loss, and an experiment was conducted to study the addition of a waiting period between deposition and gas quenching. The waiting time would allow some excess solvent to evaporate, while not yet reaching the saturation period. Control samples were allowed to completely dry without the introduction of gas quenching. After 2 min the solution started drying, resulting in the formation of the previously presented fiber-like structures. Five samples were produced with a waiting time varying from 90 to 0 s, for a total of 60 solar cells. Samples N2 2A, 2B, 2C, 2D, and 2D had waiting times of 90, 60, 30, 10 and 0 s, respectively. Their performance is presented in Table 3.

The higher pressure resulted in faster crystallization, taking around 15 s of gas flow exposure until no further color change could be observed. As expected, this resulted in higher efficiencies when compared to the lower pressure
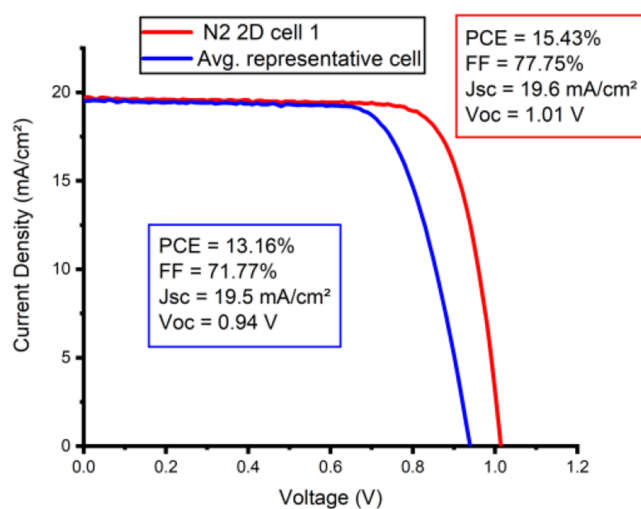

Fig. 10. J–V curve of champion and average-representative cells obtained with high pressure gas quenching and 0.5 M solution. For the average-representative cell, the one with closest performance to the average values was chosen.

gas quenched cells. Moreover, samples with higher waiting times resulted in lower apparent transparency, and samples with low waiting time exhibit visible flowing patterns due to movement of the solution caused by the gas flow. Despite these visual changes, all cells had similar performances, with no linear relation between efficiency
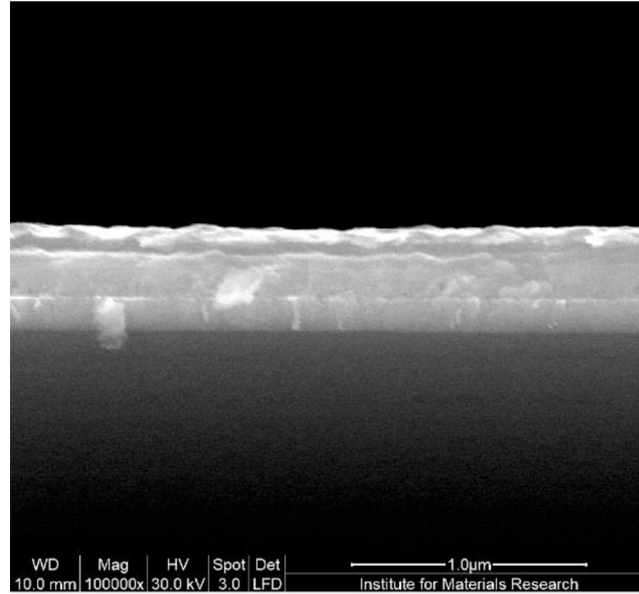
Fig. 11. Cross section of a perovskite solar cell fabricated by USSC and high pressure gas quenching, with 0.5 M solution.

Table 4. Average performance of perovskite solar cells fabricated by USSC and high pressure gas quenching, with 1 M solution (with standard deviation).

Sample	V_{oc} (mV)	J_{sc} (mA/cm^2)	FF (%)	η (%)
N2 3A	1060 ± 07	18.8 ± 0.7	71.4 ± 3.5	14.2 ± 0.8
N2 3B	1067 ± 10	17.6 ± 1.9	76.7 ± 1.6	14.4 ± 1.5
N2 3C	1060 ± 06	18.0 ± 1.0	75.6 ± 1.6	14.5 ± 0.9
N2 3D	1064 ± 07	20.0 ± 1.1	74.0 ± 2.7	15.7 ± 0.5
N2 3E	1012 ± 18	21.3 ± 0.6	74.1 ± 1.47	15.9 ± 0.5

and waiting time. The average PCE for was 13.16% ($\sigma = 0.81\%$) while the top performing cell had PCE = 15.43%, $V_{oc} = 1.01$ V, $J_{sc} = 19.6$ mA/cm^2, FF = 77.75% (sample N2 2D, cell 1) (Fig. 10).

While analyzing the samples with SEM, it was possible to verify that the higher pressure created thinner perovskite films of only 200 nm between the 150 nm ITO and 100 nm Cu layers (Fig. 11). The strategy to increase this thickness was to increase the concentration of the solution to 1 M. While being close to the 1.33 M used in spin coating, the total amount of solution per sample is still 6 times lower (17 vs 100 μl, for a 3×3 cm sample). Five samples were produced with the new solution, for a total of 60 cells. Their *J-V* measurements are presented in Table 4.

The new concentration resulted in an overall increase in performance. Although with more variation between samples, the cells presented characteristics in line with spin coated ones, with V_{oc} over 1.0 V, J_{sc} higher than 20 mA/cm^2 in some cases. The average PCE was 14.94% ($\sigma = 0.84\%$) and the top performing cell had PCE = 16.88%, $V_{oc} = 1.04$ V, $J_{sc} = 21.2$ mA/cm^2, FF = 76.46%
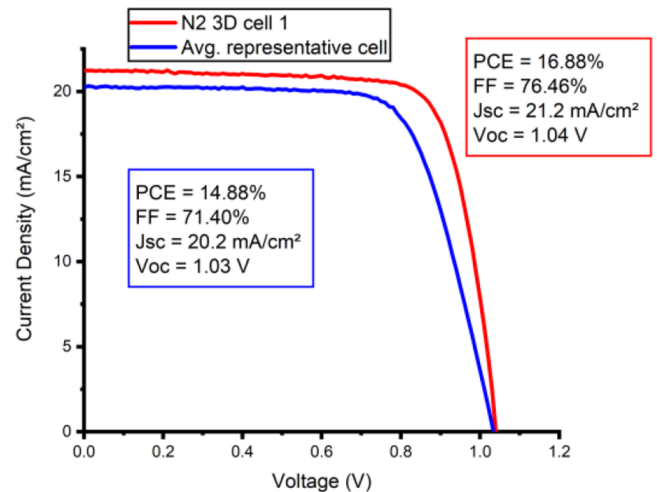

Fig. 12. *J–V* curve of champion and average-representative cells obtained with high pressure gas quenching and 1 M solution. For the average-representative cell, the one with closest performance to the average values was chosen.
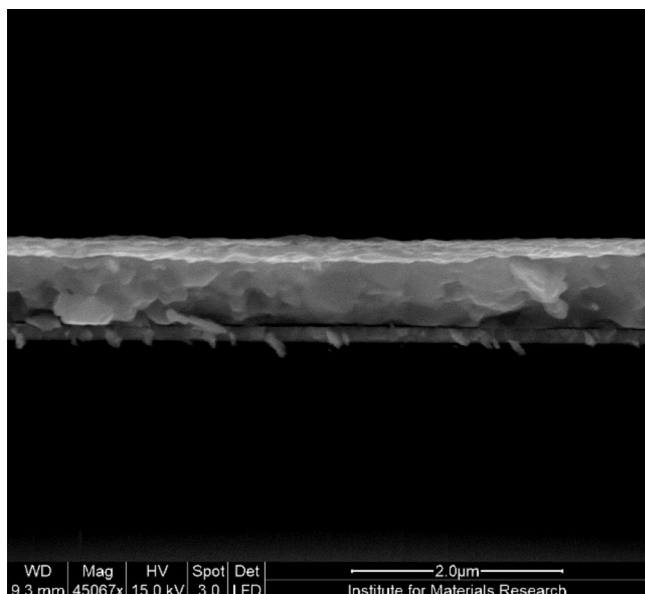
Fig. 13. Cross section of a perovskite solar cell fabricated by USSC and high pressure gas quenching, with 1 M solution.
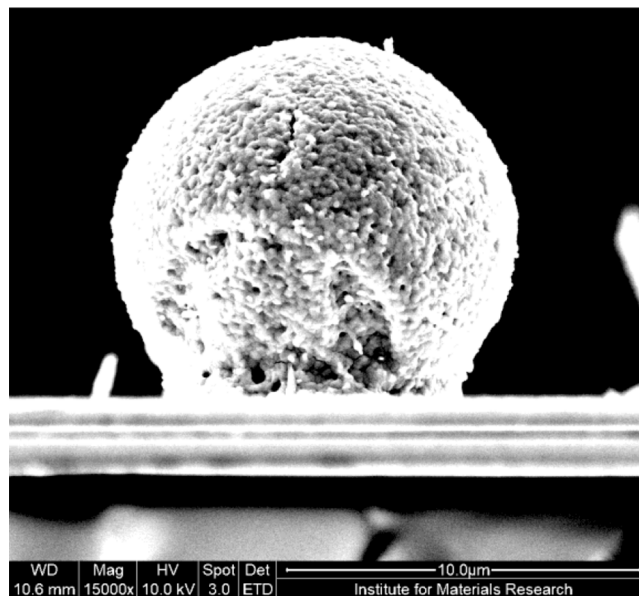

Fig. 14. Spherical defect on top of a perovskite layer deposited by USSC and gas quenching.

Table 5. Summary of the champion cell efficiencies obtained with different quenching techniques.

Quenching technique	Crystallization time (s)	Champion cell PCE (%)
Vacuum	120	8.3
Gas (low P)	25	13.3
Gas (high P)	15	16.9

(sample N2 3D, cell 1) (Fig. 12). Cross section SEM confirmed the expected thickness increase on the perovskite layer, which was approximately 620 nm thick, on top of the same 150 nm thick ITO layer (Fig. 13).

On top of the optimizations on the gas quenching and film morphology, SEM imaging also revealed the presence of spherical surface defects on the perovskite layer (Fig. 14) caused by material agglomeration. The defects do not cause any cell to be shunted, possibly due to the conformal deposition of the ETL and electrode on top of these defects. Nonetheless, the causes for the agglomeration are being studied, as it is believed that eliminating those defects could increase cell performance and stability.

4 Conclusions

With the results obtained in this work, it is clear that the ultrasonic spray coating is suited for scaling up the fabrication of perovskite solar cells. Similar characteristics were achieved in regard to complete coverage and thickness, with 600 nm thick perovskite layers being successfully integrated in complete stacks of single junction solar cells. With the use of gas quenching, it was possible to reach high efficiencies, with top performing cell having PCE = 16.88%, V_{oc} = 1.04 V, J_{sc} = 21.2 mA/cm^2, and FF = 76.46%. Moreover, the techni-

que ultimately resulted in efficiency higher than 14% across multiple cells. Ultrasonic spray coating also allows for less material consumption, having lower ink concentrations and, especially, requiring less solution per sample. This is due to the fact that all the ink being applied to the substrate, while in the spin coating technique a large part of it is projected off the substrate.

The quality and opto-electrical properties of the final perovskite film are associated mostly with the crystallization step, which occurs after the deposition of the precursor ink. By comparing different quenching techniques, it was possible to verify a dependance of the cell performance on the crystallization time. Faster quenching resulted in higher film quality and more efficient solar cells. This dependence was observed not only by comparing vacuum and gas quenching, but also when an increase in gas pressure resulted in a reduction of 10 seconds in the crystallization time (Tab. 5).

Further improvement on the crystallization time could be accomplished by the introduction of plasma quenching, which was reported to generate crystalline perovskite films with a single pass (less than 1 s exposure for a 3 cm long sample) [16]. The technique can also be used with ultrasonic spray coating. These processes represent significant improvements in cost efficiency and consume less raw material, if compared to the anti-solvent

technique, still used in laboratory scale. Another route for improvement can be the exploration of different perovskite compositions and cell architecture [25] or introduction of passivation layers and interlayers [26].

The cells produced with ultrasonic spray coating were designed for compatibility with tandem applications and deposition on rough surfaces. A natural next step of this research is, hence, integration with CIS bottom cells in monolithic tandem devices. Alternatively, perovskite-on-kesterite show great potential. CZTSSe kesterites have achieved >12% PCE [27], with the advantage of using earth abundant, non-toxic and cheaper materials than CIGS technology. Kesterites can also be solution processed and are suited for tandem applications with perovskite solar cells due to band gap matching [28].

Author contribution statement

Joao Silvano, Bart Vermang and Wim Deferme conceived and planned the project. Joao Silvano carried out the experiments, JV measurements, optical and laser imaging, and analyzed the results. Jacopo Sala performed EQE measurements and contributed to the interpretation of the results. Tamara Merckx, Yinghuan Kuang and Tom Aernouts contributed to the planning of experiments and interpretation of the results. Pieter Verding and Jan D'Haen performed the SEM measurements and contributed to the interpretation of the results. Bart Vermang and Wim Deferme supervised the project. Joao Silvano took the lead in writing the manuscripts. All authors provided critical feedback and helped shape the research, analysis and manuscript.

References

1. T. Feurer, A.N. Tiwari, Adv. Energy Mater. **9**, 1901428 (2019)
2. A. Al-Ashouri, E. Köhnen, S. Albrecht, Science **370**, 13000 (2020)
3. A. Al-Ashouri, A. Magomedov, S. Albrecht, Energy Environ. Sci. **12**, 3356 (2019)
4. G.E. Eperon, T. Leijtens, M.D. McGehee, H.J. Snaith, Science **354**, 861 (2016)
5. W. Shockley, H.J. Queisser, J. Appl. Phys. **32**, 510 (1961)
6. M. Hutchins, pv magazine (Online), 21 December 2020. Available: www.pv-magazine.com/2020/12/21/oxford-pv-retakes-tandem-cell-efficiency-record/. [Accessed on 28 June 2021].
7. Z. Li, H. Zhou, Q. Chen, Joule **2**, 1559 (2018)
8. NREL (online). Available: www.nrel.gov/pv/hybrid-tandem-solar-cells.html [Accessed on 28 June 2021]
9. J. Werner, B. Niesen, C. Ballif, ACS Energy Lett. **1**, 474 (2016)
10. M.T. Hörantner, H.J. Snaith, Energy Environ. Sci. **10**, 1983 (2017)
11. O. Shargaieva, E. Unger, Mater. Adv. **1**, 3314 (2020)
12. D.T. Moore, U. Wiesner, L.A. Estroff, J. Am. Chem. Soc. **137**, 2350 (2015)
13. A. Babaygit, J. D'Haen, H.-G. Boyen, B. Conings, Joule **2**, 1205 (2018)
14. L. Gu, S. Wang, N. Yuan, J. Ding, ACS Appl. Mater. Interfaces **14**, 2949 (2022)
15. Y. Yu, H. Yu, M. Zhang, Sol. RRL **5**, 2100386 (2021)
16. N. Rolston, W.J. Scheideler, A.C. Flick, et al. Joule **4**, 2675 (2020)
17. J.E. Bishop, J.A. Smith, D.G. Lidzey, ACS Appl. Mater. Interfaces **12**, 48237 (2020)
18. H. Chen, X. Pan, Y. Ding, S. Dai, J. Power Sources **402**, 82 (2018)
19. M. Ramesh, C.-W. Chu, ACS Appl. Mater. Interfaces **7**, 2359 (2015)
20. K. Amratisha, P. Kanjanaboos, Opt. Mater. Express **10**, 1497 (2020)
21. J. Riemer, Ultrasonic spray coating of nanoparticles, Global Solar Technology **2**, 33 (2011)
22. T. Feurer, Ph.D. thesis, ETH Zurich, 2019
23. X.-X. Gao, Y. Zhang, Y. Feng, M.K. Nazeeruddin, Adv. Mater. **32**, 1905502 (2020)
24. L. Krückemeyer, U. Rau, M. Stolterfoht, T. Kirchartz, Adv. Energy Mater. **10**, 1902573 (2019)
25. J.E. Bishop, D.G. Lidzey, Sci. Rep. **10**, 6610 (2020)
26. H. Min, G. Kim, T.J. Shin, S.I. Seok, Nature **598**, 444 (2021)
27. W. Wang, M.T. Winkler, O. Gunawan, et al. Adv. Energy Mater. **4**, 1301465 (2014)
28. Y. Li, N. Yuan, J. Dind, Solar Energy **155**, 35 (2017)